



SARS-CoV-2 nsp15 enhances viral virulence by subverting host antiviral defenses

Allen Caobi^{a,b} , Chia-Ming Su^{a,b} , Christian M. Beusch^{c,d}, Devin Kenney^{a,b}, Tamarand L. Darling^{e,f,g}, Shuchen Feng^h, Marc Semaan^{a,b} , Alan Wacquez^{a,b}, Nathan L. Sanders^{i,j}, Ena S. Tully^k, Da-Yuan Chen^{a,b} , Monika Evdokimova^h, Zhen Ding^{a,b}, Dakota Jones^{l,m}, Konstantinos-Dionysios Alysandratos^{i,l,m}, Joseph P. Mizgerd^{b,i,j,m}, Robert N. Kirchdoerfer^k , Darrell N. Kotton^{i,l,m} , Florian Douam^{b,j}, Nicholas A. Crossland^{b,j,n} , Adrianus C. M. Boon^{e,f,g} , David E. Gordon^c, Susan C. Baker^h , and Mohsan Saeed^{a,b,1}

Affiliations are included on p. 10.

Edited by Peter Sarnow, Stanford University School of Medicine, Stanford, CA; received December 19, 2024; accepted May 9, 2025

SARS-CoV-2 encodes numerous virulence factors, yet their precise mechanisms of action remain unknown. We provide evidence that the SARS-CoV-2 nonstructural protein 15 (nsp15) enhances viral virulence by suppressing the production of viral double-stranded (dsRNA), a potent inducer of antiviral signaling. The viral variants lacking nsp15 endoribonuclease activity elicited higher innate immune responses and exhibited reduced replication in human stem cell–derived lung alveolar type II epithelial cells, as well as in the lungs of infected hamsters. Consistently, these variants caused significantly less weight loss and mortality compared to wild-type (WT) virus in K18-hACE2 mice. Mechanistically, the cells infected with nsp15 mutants accumulated more viral dsRNA, causing enhanced stimulation of the interferon pathway. Chemical inhibition of interferon signaling dampened immune responses to nsp15 mutants and restored their replication to levels similar to the WT virus. These findings indicate that the endoribonuclease activity of nsp15 contributes to viral virulence by limiting the accumulation of viral dsRNA, thereby allowing robust replication with reduced activation of the host innate immune response.

Severe acute respiratory syndrome coronavirus 2 (SARS-CoV-2) has an exceptional ability to overcome host defense barriers. It encodes a range of highly specialized proteins that work in concert with each other to neutralize host antiviral pathways at multiple stages, creating an intracellular environment conducive for viral replication. A deeper understanding of how each of these proteins contributes to immune evasion will enhance our knowledge of viral pathogenesis and guide the development of effective disease management strategies, including the design of attenuated viruses as potential vaccine candidates. This study addresses the function of the SARS-CoV-2 nonstructural protein 15 (nsp15) in innate immune antagonism and viral pathogenesis.

The SARS-CoV-2 genome comprises approximately 30,000 nucleotides. The 5' two-thirds of the viral genome contains two large, partially overlapping open reading frames, ORF1a and ORF1b, which are translated by host ribosomes into two polyproteins, pp1a and pp1ab, respectively. These polyproteins are cotranslationally processed by two viral proteases, nsp3 (also called papain-like protease or PL^{pro}) and nsp5 (also called 3-chymotrypsin-like protease or 3CL^{pro}), resulting in the release of 16 nonstructural proteins (nsp1–16). Together, these nsps orchestrate the assembly of the replication–transcription complex (RTC), which localizes to double-membrane vesicles (DMVs), also known as replication organelles, that serve as the site for viral RNA synthesis (1, 2). Proteins generated from the 3' end of the genome enhance viral replication through various indirect mechanisms, such as co-opting host factors or antagonizing host innate defenses, and enable the assembly of mature virus particles.

Nsp15 is an essential viral protein, highly conserved across coronaviruses (3, 4). Studies have shown that it is a component of the coronaviral RTC (5, 6), and recent computational modeling suggests that it may actually serve as a scaffold for RTC assembly (7). Additionally, nsp15 from various coronaviruses—including porcine epidemic diarrhea virus (PEDV), mouse hepatitis virus (MHV), infectious bronchitis virus (IBV), SARS-CoV, Middle East respiratory syndrome coronavirus (MERS-CoV), and most recently SARS-CoV-2, has been demonstrated to delay the activation of the interferon (IFN) pathway in infected cells, primarily by preventing the accumulation of viral double-stranded RNA (dsRNA) through its endoribonuclease activity (8–13). In vivo experiments with PEDV, MHV, and IBV demonstrated that nsp15 is a critical virulence factor—viral variants lacking the nsp15 endoribonuclease activity caused milder disease and were rapidly cleared (8, 9, 12). These findings highlight the critical role of nsp15 during coronaviral infections.

Significance

Severe acute respiratory syndrome coronavirus 2 (SARS-CoV-2) employs multiple strategies to evade human antiviral defenses, leading to potentially severe outcomes such as pneumonia and death. A detailed investigation of these evasion strategies should enhance our understanding of SARS-CoV-2 pathogenesis and guide future vaccine development. In this study, we focus on the SARS-CoV-2 nonstructural protein 15 (nsp15) and demonstrate that its endoribonuclease activity delays the activation of antiviral responses in human lung cells. SARS-CoV-2 variants lacking this activity exhibit impaired replication and cause milder disease in animals, highlighting nsp15 as a key virulence factor. These findings underscore the importance of nsp15's endoribonuclease activity in both promoting virus replication and influencing disease severity.

Author contributions: D.K., J.P.M., R.N.K., D.N.K., F.D., A.C.M.B., D.E.G., S.C.B., and M.Saeed designed research; A.C., C.-M.S., C.M.B., D.K., T.L.D., M. Semaan, A.W., N.L.S., E.S.T., D.-Y.C., M.E., Z.D., D.J., K.-D.A., R.N.K., and D.E.G. performed research; C.M.B., D.K., T.L.D., S.F., N.A.C., A.C.M.B., S.C.B., and M. Saeed analyzed data; J.P.M. provided expertise in lung biology; and A.C. and M.Saeed wrote the paper.

The authors declare no competing interest.

This article is a PNAS Direct Submission.

Copyright © 2025 the Author(s). Published by PNAS. This open access article is distributed under [Creative Commons Attribution-NonCommercial-NoDerivatives License 4.0 \(CC BY-NC-ND\)](https://creativecommons.org/licenses/by-nc-nd/4.0/).

¹To whom correspondence may be addressed. Email: msaeed1@bu.edu.

This article contains supporting information online at <https://www.pnas.org/lookup/suppl/doi:10.1073/pnas.2426528122/-/DCSupplemental>.

Published June 12, 2025.

Nsp15 has three domains: the N-terminal domain (NTD), essential for protein oligomerization, the middle domain (MD), involved in interactions with other viral proteins, and the C-terminal domain (CTD), which harbors the endoribonuclease activity (4, 14). Biochemical assays with recombinant nsp15 have shown that it preferentially cleaves RNA substrates 3' of uridines, earning it the name of endoU (4, 15, 16). The conservation of endoU across a wide range of coronaviruses underscores its essential functions in the viral lifecycle and pathogenesis, yet the relevance of endoU to SARS-CoV-2 pathogenesis is yet to be defined.

Biochemical and structural studies have provided important insights into SARS-CoV-2 endoU (14, 17, 18). The cryoelectron microscopy (Cryo-EM) reconstruction of nsp15 bound to UTP revealed that, similar to other coronaviruses (19), SARS-CoV-2 nsp15 assembles into a homohexamer. The NTD mediates oligomerization by forming two head-to-head stacked trimers, with the endoU domains facing outward (14). The endoU is only active when in its hexameric form, although these observations are yet to be confirmed in virus-infected cells. The endoU active site consists of a catalytic triad—two histidines (H234 and H249) and a lysine (K289)—which catalyzes RNA cleavage via the characteristic acid–base reaction. This yields a single 3' cleavage product (5'-OH-RNA) and a mixture of two 5' cleavage products (RNA-2'3'-cyclic phosphate and RNA-3'-phosphate) (14). The uridine specificity of endoU is primarily driven by a conserved serine (S293) within the uridine-binding pocket (14, 20, 21). While structural studies, biochemical assays, and molecular dynamics have detailed endoU's enzymatic mechanism, they provide no insight into its functions during SARS-CoV-2 infection.

While our work was in progress, Otter et al. demonstrated that a recombinant SARS-CoV-2 with inactive endoU triggers an enhanced innate immune response in cell culture and replicates less efficiently in primary nasal epithelial cells, highlighting endoU's role in innate immune evasion (13). However, the in vivo relevance of these findings remains unexplored. We generated SARS-CoV-2 variants with mutations in the endoU catalytic site as well as in a motif associated with nsp15's uridine specificity and tested the replication and pathogenic potential of these variants in cell culture systems and animal models. Our results suggest that SARS-CoV-2 nsp15 is a critical virulence factor, enabling the virus to evade innate defense mechanisms in the respiratory tract and thereby facilitating viral infection and pathogenesis.

Results

Generation of SARS-CoV-2 Variants Containing nsp15 Mutations.

To assess the functions of the nsp15 endoU activity during SARS-CoV-2 infection, we aimed to generate viral variants containing alanine substitutions at each of the three catalytic site residues, H234, H249, and K289. These residues are highly conserved across coronaviruses (Fig. 1 *A* and *B*), and their replacement with alanine has been shown to disrupt the endoU activity (14, 22–24). Additionally, we chose S293, an amino acid implicated in endoU's uridine specificity (14, 17, 25), for substitution with alanine. While we successfully generated the SARS-CoV-2 H234A, K289A, and S293A variants, we were unable to recover the H249A variant despite multiple attempts. Further analysis revealed that the H249A genome replicated minimally in producer cells, around 2,000-fold lower than the wild-type (WT) virus, potentially limiting the production of infectious virus particles (SI Appendix, Fig. S1A). Similarly, no virus particles were recovered when we replaced H249 with other small amino acids, such as glycine or serine. However, substitution with the positively charged amino acid arginine (H249R) was successful, although the virus

titer was approximately 10-fold lower ($P < 0.05$) than that of the WT virus (SI Appendix, Fig. S1B). These findings suggest that histidine at position 249 may play a critical role in nsp15 folding or in protein–protein/protein–RNA interactions, leading us to exclude this amino acid from further analysis.

Biochemical assays showed that catalytic site substitutions H234A and K289A abolished nsp15's ability to cleave a synthetic single-stranded RNA (ssRNA) substrate (SI Appendix, Fig. S2). In contrast, S293A retained significant RNA cleavage activity under saturating conditions, but, like the other mutants, failed to cleave RNA when a 10-fold excess of substrate was used, indicating that the S293A substitution reduces but does not abolish the endoU activity. All nsp15 variants were purified as hexamers, indicating the mutations did not disrupt oligomerization (SI Appendix, Fig. S3).

The SARS-CoV-2 endoU Mutants Replicate as Efficiently as WT Virus in Vero E6 Cells.

The successful generation of recombinant H234A, K289A, and S293A variants suggests that both the endoU activity and uridine specificity of nsp15 are dispensable for core replication processes of SARS-CoV-2. To confirm, we examined the growth kinetics of nsp15 variants in Vero E6 cells, which lack type I IFN production (26, 27) and therefore allow evaluation of virus replication in the absence of robust innate immune pressures. All nsp15 variants replicated to the same level as WT virus, with similar nucleocapsid (N)-positive cell percentages and comparable viral titers at 48 and 72 h postinfection (hpi) (Fig. 1 *C* and *D*). Western blot analysis revealed equivalent N levels in cells infected with all viruses (Fig. 1*E*). Importantly, no difference in nsp15 abundance was observed between WT and nsp15 mutant-infected cells (Fig. 1*E*), indicating the mutations did not impair nsp15 production or stability. Finally, all endoU mutants formed plaques with diameters similar to those of WT virus (SI Appendix, Fig. S1C). These findings suggest that the endoU activity of nsp15 is dispensable for efficient virus replication in an immune-deficient environment.

The endoU Catalytic Mutants Replicate Poorly in Human Stem Cell-Derived Lung Alveolar Epithelial Cells.

Alveolar type II epithelial (AT2) cells are a primary target of SARS-CoV-2 infection in the human lungs (28). We previously reported that human induced pluripotent stem cell–derived AT2 (iAT2) cells are permissive to SARS-CoV-2 infection and respond by mounting a strong IFN response (29, 30). To test whether nsp15 promotes viral infection in an immune-competent environment, we infected iAT2 cells in air–liquid interface (ALI) cultures with nsp15 mutants and compared their replication to WT virus by measuring viral titers on the apical side of cells. The nsp15 catalytic mutants, H234A and K289A, showed attenuated replication, with titers 8.4- and 20-fold lower than WT virus at 72 hpi, and 6.35- and 39.2-fold lower at 96 hpi, respectively (Fig. 1*F*). In contrast, the S293A mutant replicated similarly to WT virus, suggesting either the S-to-A change did not impair nsp15's uridine specificity, the uridine specificity is not essential for virus replication in iAT2 cells, or the lower level of endoU activity of this mutant is sufficient for RNA processing during infection. Collectively, these findings indicate that nsp15's endoU catalytic activity plays a critical role in SARS-CoV-2 infection in immune-competent cells.

The endoU Catalytic Mutants Elicit an Elevated Innate Immune Response in iAT2 Cells.

We hypothesized that the reduced replication of endoU catalytic mutants in iAT2 cells resulted from their diminished ability to effectively suppress the antiviral innate immune response. To test this, we performed global transcriptomic analyses of iAT2 cells infected with our panel of recombinant

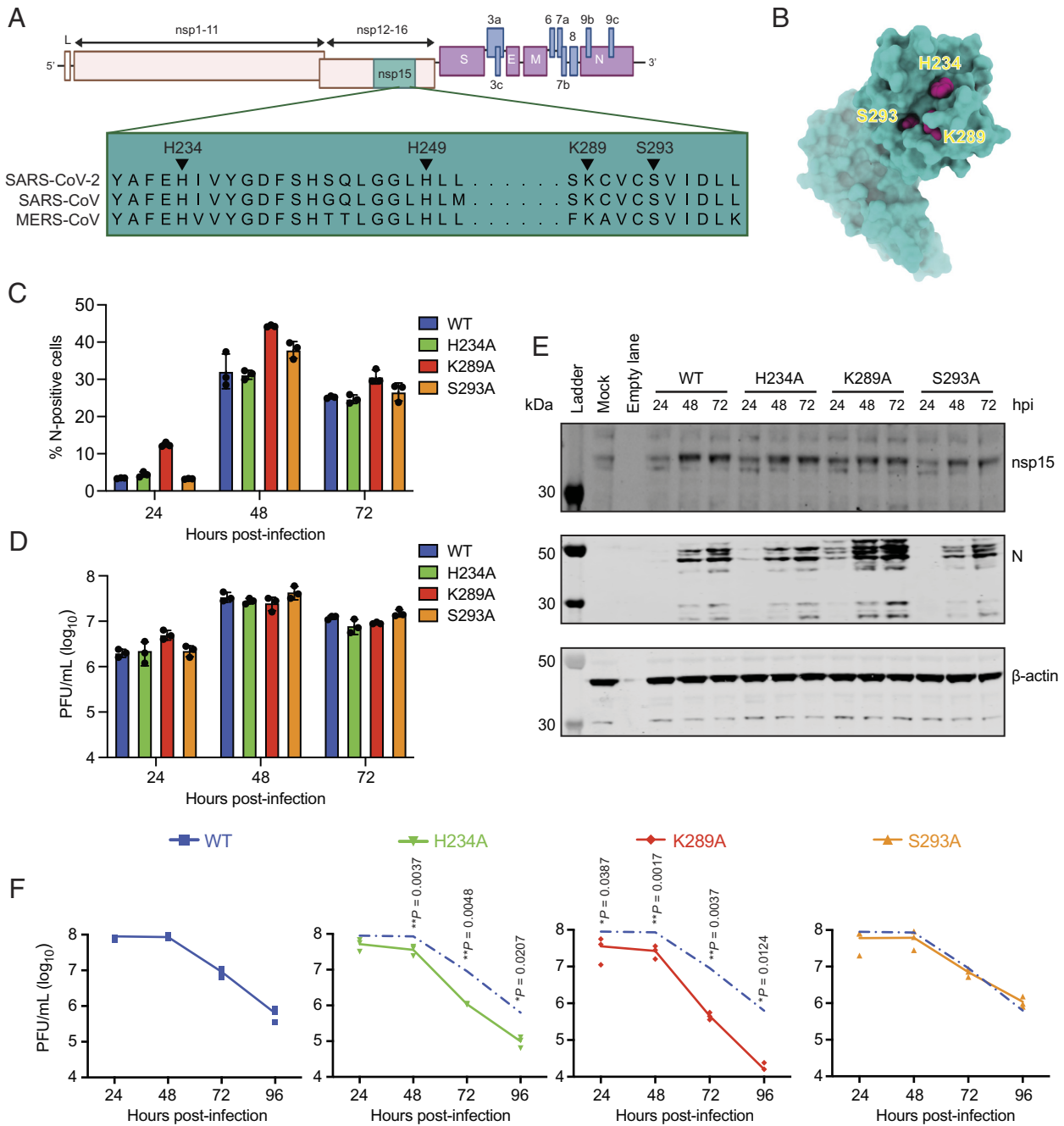


Fig. 1. EndoU catalytic mutants replicate to the same level as WT virus in Vero E6 cells but are attenuated in iAT2 cells. (A) Schematic representation of the SARS-CoV-2 genome. Nsp15 is highlighted in green. The *Bottom* panel shows amino acid sequence alignment of endoU active site residues from nsp15 homologs. Three active site residues (H234, H249, and K289) and a residue critical for the endoU specificity of the protein (S293) are indicated with arrowheads. (B) Critical active site residues are projected on the tertiary structure of an nsp15 protomer. (C) Vero E6 cells infected at an MOI of 0.1 were analyzed by flow cytometry. The percentage of N-positive cells is shown. (D) Viruses egressed from infected Vero E6 cells in C were titrated by the plaque assay on Caco-2/AT cells. (E) Cell lysates from Vero E6 cells in C were analyzed by western blot. (F) iAT2 cells, grown as ALI cultures, were infected on the apical side at an MOI of 0.3. Virus titer in apical washes collected at indicated times was measured by the plaque assay on Caco-2/AT cells. Statistical significance was determined using the two-tailed parametric *t* test.

viruses at 24 and 48 hpi. Principal component analysis revealed that the nsp15 catalytic mutants H234A and K289A formed a distinct cluster, separate from WT virus, at 24 hpi, with this difference becoming more pronounced at 48 hpi (*SI Appendix, Fig. S4A*). In contrast, S293A and WT virus clustered together, indicating similar gene expression patterns. Consistently, H234A and K289A induced more differentially expressed genes (DEGs) than S293A when compared to WT virus (*SI Appendix, Fig. S4B*).

Gene Ontology (GO) analysis showed that most of these DEGs belonged to the pathways implicated in host responses to viral infections (*SI Appendix, Fig. S5*). Specifically, genes in the “Defense

Response to Virus” (Gene Ontology Group: 0051607) were significantly more upregulated by H234A and K289A than WT virus, while S293A showed no notable differences (Fig. 2A). Many of these antiviral genes, including interferons (IFNs) (e.g., IFNB1, IFNL1, IFNL2, IFNL3) and interferon-stimulated genes (ISGs) (e.g., IFIT1-3, IFITM1-3, OAS1-3, ISG15, RSAD2, BST2, MX1/2, ZBP1) were also upregulated in WT virus-infected cells, though to a lesser extent. We confirmed these findings by RT-qPCR analysis of select ISGs (Fig. 2B and *SI Appendix, Fig. S6*).

In addition to antiviral genes, several inflammatory factors (e.g., CXCL3, CXCL5, CXCL10, CXCL11, IL6, CCL5, CCL20,

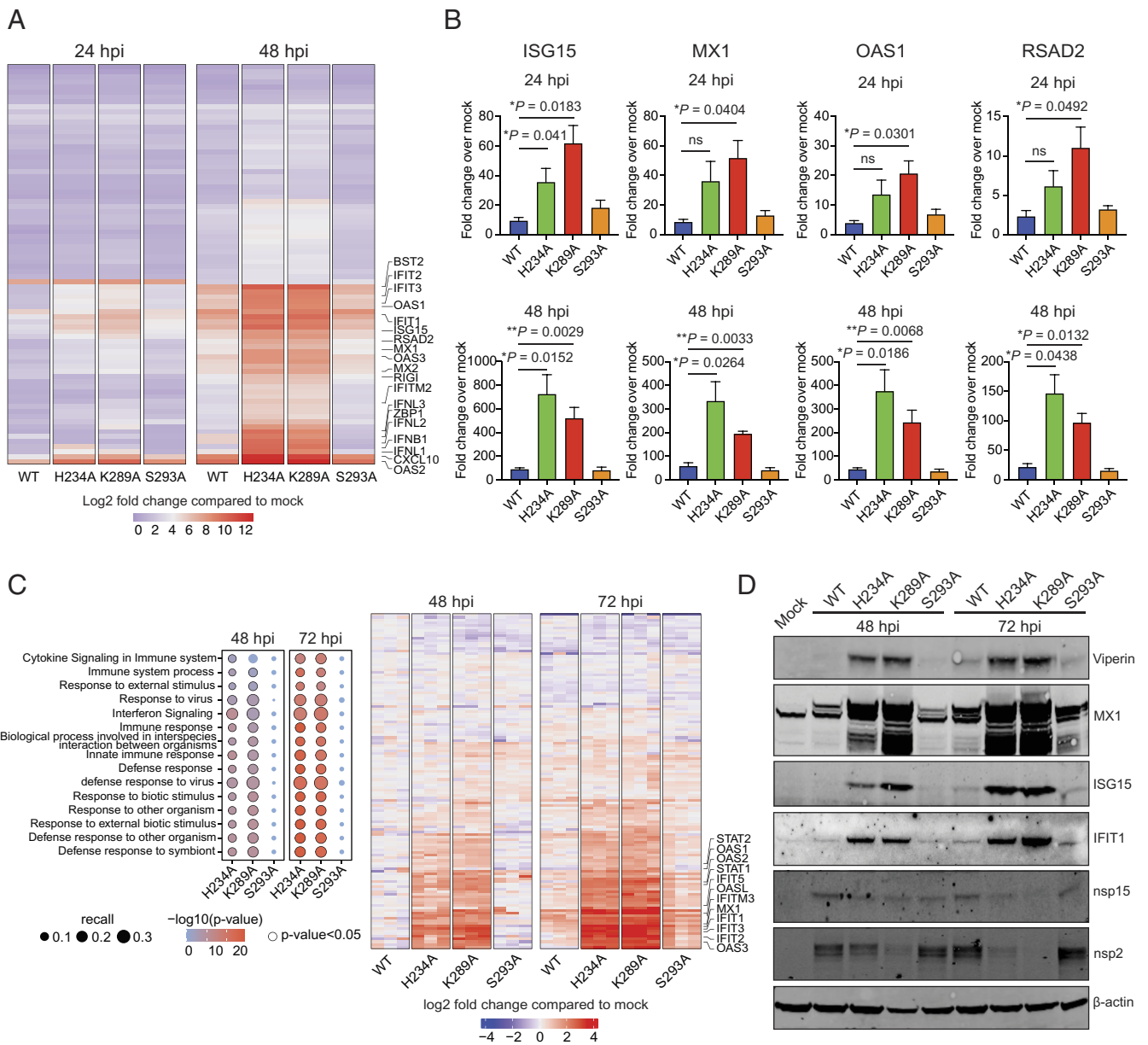


Fig. 2. EndoU catalytic mutants induce an elevated innate immune response in iAT2 cells. (A) RNA extracted from iAT2 cells infected with indicated viruses at an MOI of 0.3 was subjected to mRNA sequencing. The heatmap represents the Gene Ontology group, “Defense Response to Virus” (GO: 0051607). Some representative genes differentially regulated by H234A and K289A viruses are listed. (B) Indicated ISGs were quantified in infected iAT2 cells (MOI, 0.3) by RT-qPCR. Statistical significance was determined using the two-tailed parametric t test. (C) iAT2 cells infected with indicated viruses (MOI: 0.3) were analyzed for global proteomic analysis. The *Left* panel shows the Gene Ontology groups differentially regulated by nsp15 mutants compared to the WT virus. The *Right* panel shows the heatmap generated for the Gene Ontology group, “Defense Response to Virus” (GO: 0051607). Some representative genes differentially regulated by H234A and K289A viruses are listed. (D) Cell lysates prepared from infected iAT2 cells (MOI: 0.3) were analyzed by western blot for indicated proteins.

SOCS1, CSF3, MMP13) were also more strongly elicited in H234A and K289A infections compared to WT, suggesting endoU activity also delays the inflammatory response to infection. Together, these findings indicate that endoU regulates antiviral and inflammatory responses, potentially preventing excessive tissue damage. This aligns with reports that coronavirus endoU activity facilitates viral evasion of host sensors (10, 11).

We next performed a global proteomic analysis of infected cells to examine immune responses at the protein level. Consistent with the transcriptomics data, H234A and K289A viruses, but not S293A, triggered an earlier and more robust innate immune response compared to WT virus (Fig. 2C), an observation we subsequently confirmed by western blot (Fig. 2D). Notably, viral nsp2 and nsp15 levels were lower in H234A and K289A-infected cells (Fig. 2D), aligning with the poor replication of these variants in

iAT2 cells. Together, these results indicate that SARS-CoV-2 with catalytically inactive endoU is less effective at facilitating evasion of host innate immune responses.

The Active-Site endoU Mutants Are Attenuated in K18-hACE2

Mice. Given the lower replication of nsp15 catalytic mutants in iAT2 cells, we tested their replication and virulence in vivo. For this, we first intranasally infected K18-hACE2 transgenic mice expressing human angiotensin converting enzyme 2 (hACE2) (8 mice per virus) with 1×10^4 plaque-forming units (PFU) and monitored weight loss and survival. By 7 d postinfection (dpi), 6/8 mice infected with WT virus and 5/8 with S293A lost over 20% of body weight, while only 3/8 for H234A and 1/8 for K289A showed similar weight loss (Fig. 3A). Survival rates were 75 and 87.5% for H234A and K289A, compared to 25 and 37.5% for

WT virus and S293A (Fig. 3B), suggesting that nsp15 catalytic mutants are less virulent.

Next, we investigated the replication kinetics of WT, H234A, and K289A viruses in the lungs and brain of K18-hACE2 mice. For this, 18-wk-old mice were intranasally inoculated with 5×10^3 PFU (12 mice per virus), and viral load in the lungs and brain was measured at 2 and 6 dpi. We selected 6 dpi because neuroinvasion in K18-hACE2 mice typically occurs after six days of infection with the used inoculum size. Consistent with our *in vitro* results, the viral titer and RNA copy number in the lungs of WT-infected mice were higher than those in H234A and K289A-infected animals at 2 dpi (Fig. 3C and D). By 6 dpi, the virus was nearly undetectable in the lungs. Although no virus was detected in the brain at 2 dpi, infectious virus particles became detectable in 3/6 mice infected with the WT virus by 6 dpi, with the average viral titer of 2.84×10^7 PFU/mg of brain tissue (Fig. 3E). In contrast, the average titers in the brains of H234A and K289A-infected animals were 5.86×10^5 and 3.85×10^4 PFU/mg of brain tissue, respectively. These results indicate that nsp15 mutants replicate relatively inefficiently in the lungs of K18-hACE2 mice.

The Active-Site endoU Mutants Exhibit Reduced Replication and Enhanced Innate Immune Response in Hamsters. While hACE2 transgenic mice represent a powerful model for the study of SARS-CoV-2 virulence, the weight loss and death in these animals are linked to viral neuroinvasion (31–34). In contrast, in

Syrian hamsters, the infection is largely restricted to the respiratory system, with a similar lung pathology as in humans (31, 35, 36). To assess the role of endoU in viral replication and immune evasion in this animal model, we infected Syrian hamsters with WT virus and H234A (8 hamsters per virus) at a low dose of 1,000 PFU per animal and harvested their nasal turbinates, lungs, heart, and small intestine at 2 and 5 dpi. While uninfected animals gained body weight during the course of the experiment, the weight of infected hamsters remained unchanged, with no statistically significant difference between WT- and H234A-infected animals (SI Appendix, Fig. S7A).

The RT-qPCR and plaque assay revealed an appreciable, but statistically insignificant, decrease in both viral RNA and infectious titer in nasal turbinates of H234A-infected animals compared to WT virus-infected animals at 2 and 5 dpi (Fig. 3C and SI Appendix, Fig. S7B). However, H234A-infected animals had significantly lower viral RNA and titers in the lungs at 5 dpi. Little or no viral replication was detected in extrapulmonary tissues (Fig. 3C and SI Appendix, Fig. S7B). RT-qPCR revealed significantly elevated expression of interferon beta (IFNB1) and ISGs in the lungs of H234A-infected animals at 2 dpi (Fig. 3), which returned to baseline by 5 dpi. Correspondingly, there was a marked increase in immune cell infiltration, including neutrophils and mononuclear cells, in the lungs of three out of four hamsters infected with the H234A mutant compared to those infected with the WT virus (Fig. 4C and D and SI Appendix, Fig. S7C). The effect of the H234A substitution on viral titer and ISG expression

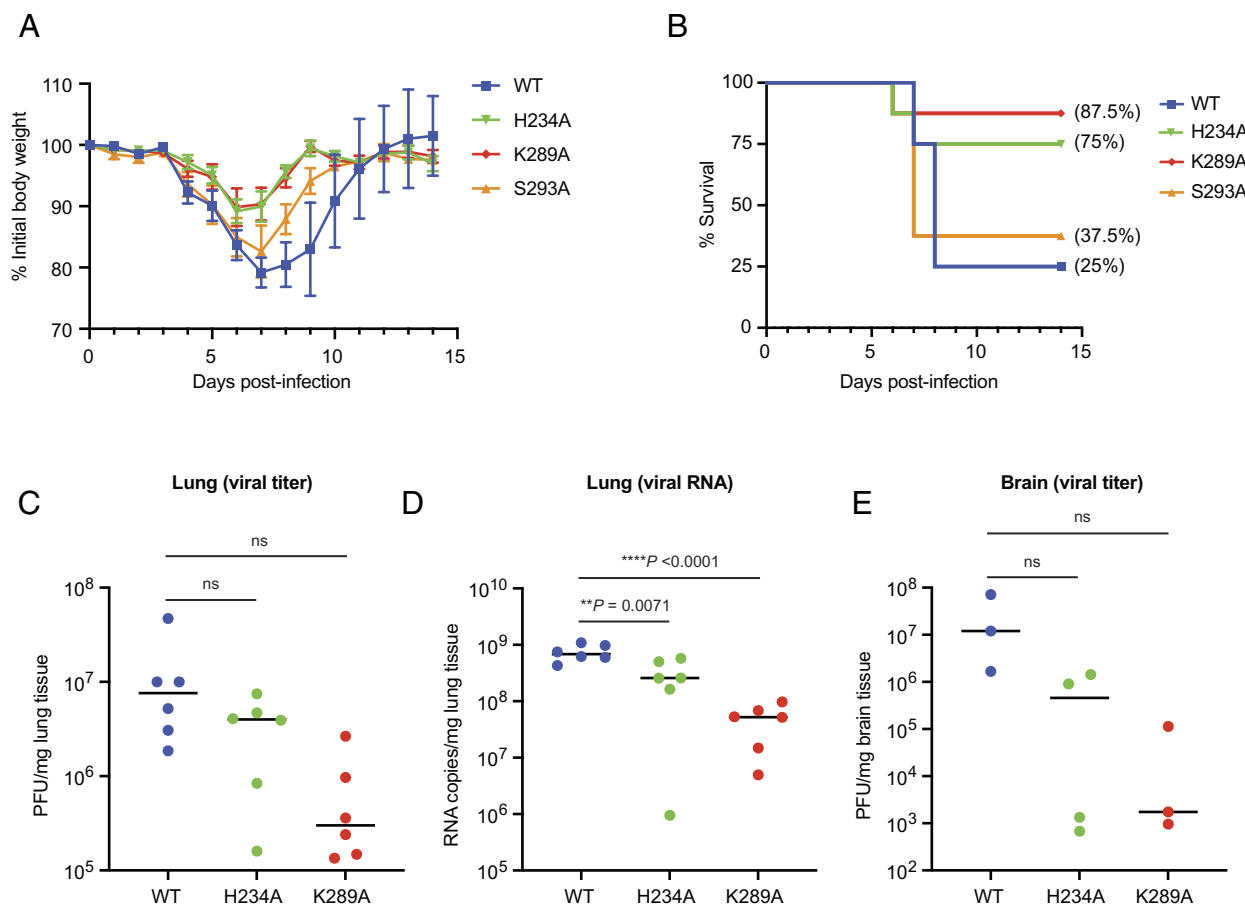


Fig. 3. EndoU catalytic mutants cause attenuated disease in K18-hACE2 mice (A and B). K18-hACE2 mice intranasally inoculated with 1×10^4 PFU/animal of indicated viruses (8 mice per virus) were monitored daily for weight loss (A) and death (B). Animals losing over 20% of their body weight were killed as per our IACUC protocols. (C–E) Male and female K18-hACE2 mice (aged 18 wk) were intranasally inoculated with 5×10^3 PFU of WT (n = 12 mice), H234A (n = 12 mice), or K289A (n = 12 mice). Lungs and brains were collected from infected mice at 2 and 6 dpi, with six mice per virus per time point, and viral titers were determined by plaque assay on Caco-2/AT cells. Shown are viral titers in the lungs at 2 dpi (C) and in brain at 6 dpi (E). Viral RNA levels in the lungs were measured at 2 dpi by RT-qPCR targeting the E gene (D). Each dot represents an infected animal. Statistical significance was determined using the two-tailed, unpaired parametric *t* test. ns, not significant.

in the lungs of infected hamsters was further confirmed in an independent experiment (*SI Appendix, Fig. S8*). In all, these findings indicate that nsp15's endoU activity promotes viral infection by facilitating the evasion of host innate immune responses in the lungs of hamsters.

Cells Infected with nsp15 Catalytic Mutants Accumulate More dsRNA. To investigate how endoU activity mediates evasion of innate immunity, we first examined whether it regulates the production of SARS-CoV-2 defective particles, known inducers of innate immune responses (37, 38). Since H234A and K289A exhibited similar effects in earlier experiments, we only focused on H234A for mechanistic studies. Our analysis revealed no significant difference between WT virus and H234A in the infectious units-to-RNA ratio, suggesting that nsp15 does not regulate defective virus particle production (*SI Appendix, Fig. S9*).

Nsp15's endoU activity is thought to minimize viral dsRNAs that serve as pathogen-associated molecular patterns (PAMPs) for innate immune induction (8, 10, 11, 13). When stained with an antibody directed against dsRNA, iAT2 cells infected with H234A showed puncta that appeared bigger than those seen in WT virus-infected cells (Fig. 5A). An unbiased analysis of over 1,000 puncta confirmed a statistically significant increase in dsRNA accumulation in H234A-infected cells, supporting endoU's role in limiting dsRNA in infected cells (Fig. 5B).

We hypothesized that increased dsRNA accumulation in H234A-infected cells enhanced IFN production, leading to elevated expression of IFN-responsive genes. Supporting this, treating iAT2 cells with JAK1/2 inhibitors Ruxolitinib and Baricitinib during virus infection completely blocked immune responses triggered by both WT and H234A viruses (Fig. 5C). Notably, under these conditions, H234A replication was restored to levels comparable to the WT virus (Fig. 5D). Similar results were obtained with the K289A mutant (*SI Appendix, Fig. S10*). JAK1/2 inhibitors block IFN-mediated STAT phosphorylation and nuclear translocation, consequently suppressing cell responsiveness to IFN without altering its production and release. Combined with our previous observation that SARS-CoV-2-infected cells exhibit reduced IFN responsiveness (30), this suggests that cells infected with endoU mutants produce more IFN, which in turn triggers ISG expression in neighboring cells, thus restricting viral spread. Overall, these findings demonstrate that SARS-CoV-2 endoU is a potent virulence factor that facilitates evasion of host IFN responses.

Discussion

We report that SARS-CoV-2 endoU is a critical virulence factor. K18-hACE2 mice infected with endoU catalytic mutants had higher survival rates compared to those infected with WT virus, likely due to reduced viral replication in the respiratory tract, which prevented neuroinvasion, the major cause of death in these mice (33, 34). This phenotype is likely driven by an earlier and stronger innate immune response in the respiratory tract, limiting viral spread to other organs. This is supported by a recent study demonstrating elevated immune responses in human airway epithelial cells infected with an endoU-deficient virus (13), and by our findings of reduced viral titers and enhanced ISG induction in the hamster lungs and human lung type II epithelial cells infected with endoU-deficient viruses. These results highlight the role of endoU in promoting viral replication by antagonizing the innate immune response.

While biochemical experiments have demonstrated the critical role of S293 in endoU's uridine specificity—the S to A substitution at this position significantly impaired the uridine specificity

(16, 17)—in our settings, the S293A substitution neither reduced virus replication nor triggered an elevated innate immune response. We propose three possible explanations for this. First, the S293 residue may not be as pivotal for nsp15's uridine specificity within infected cells. Notably, the biochemical assays involving S293 were performed in the absence of other viral proteins that normally interact with nsp15 during infection, such as nsp7, nsp8, and nsp12 (5, 39). It is possible that interaction with these proteins during infection diminishes the significance of the S293 residue in determining nsp15's uridine specificity. Second, since serine and alanine are quite similar in size, the S-to-A change may be too subtle to significantly alter endoU's preference for uridine in an infectious context. Third, uridine-specificity may not be as critical for immune-evasion functions of SARS-CoV-2 nsp15. Structural and biochemical studies indicate that other residues, including N277, W332, and Y342, also contribute to endoU's uridine specificity (16, 17, 21). A comprehensive mutational analysis of these residues, either individually or in combination, could help clarify these points.

IF analysis of cells infected with an nsp15 catalytic mutant demonstrated a significant increase in J2-reactive RNA accumulation. The precise nature of these nucleic acid molecules is unknown. It has been proposed that both dsRNA replication intermediates and negative-strand poly-U sequences act as PAMPs in coronavirus-infected cells, triggering the innate immune response via pathogen recognition receptors (PRRs), such as MDA5, RIG-I, PKR, and OAS. Nsp15 is thought to cleave these RNAs, preventing PRR activation (8, 10–13, 40). Hackbert et al. demonstrated that in MHV-infected bone marrow-derived macrophages (BMDMs), dsRNA antibody-reactive RNA molecules are negative-sense RNAs spanning the entire viral genome and that these RNAs are around 10 times more abundant in cells infected with endoU mutants compared to WT virus (10). This suggests that the negative-sense coronaviral RNA molecules may contain sequences or structures specifically recognized and cleaved by nsp15. However, Ancar et al., using cyclic phosphate cDNA sequencing, showed that endoU activity predominantly targets positive-strand viral RNA in MHV-infected BMDMs (41). Since this analysis was performed relatively late during infection (8 and 12 hpi), it may reflect nonspecific activity of nsp15. Further studies at early infection stages are needed to pinpoint endoU's specific targets and clarify its role in viral RNA processing.

In addition to serving as PAMPs for the IFN pathway, viral dsRNA also triggers other antiviral processes. For instance, coronaviral dsRNA activates PKR, a key antiviral protein (8, 11, 13, 42). Upon binding to dsRNA, PKR undergoes autophosphorylation, phosphorylates the alpha subunit of eukaryotic initiation factor 2 (eIF2 α), and induces global translation shutoff and stress granule (SG) formation, severely impairing viral replication. A recent study showed that the avian coronavirus IBV inhibits SG formation by regulating dsRNA levels via its endoU activity (42). The OAS/RNase L pathway is another defense mechanism activated by viral dsRNA. Upon dsRNA binding, OAS enzymes (isoforms 1–3) produce 2'-5'-oligoadenylates (2-5A), which activate RNase L to degrade viral and host RNAs, suppressing viral replication. MHV nsp15 is known to inhibit this pathway (8, 11). Additionally, a recent study showed that viral dsRNA in SARS-CoV-2-infected cells adopts a Z conformation, acting as a PAMP for Z-conformation nucleic acid binding protein 1 (ZBP1)(43–45). ZBP1 activation triggers PANoptosis, a cell death pathway that restricts viral replication. Our recent MHV study showed increased activation of the ZBP1 pathway in cells infected with endoU-deficient viruses compared to WT (46). We are further exploring this in the context of SARS-CoV-2.

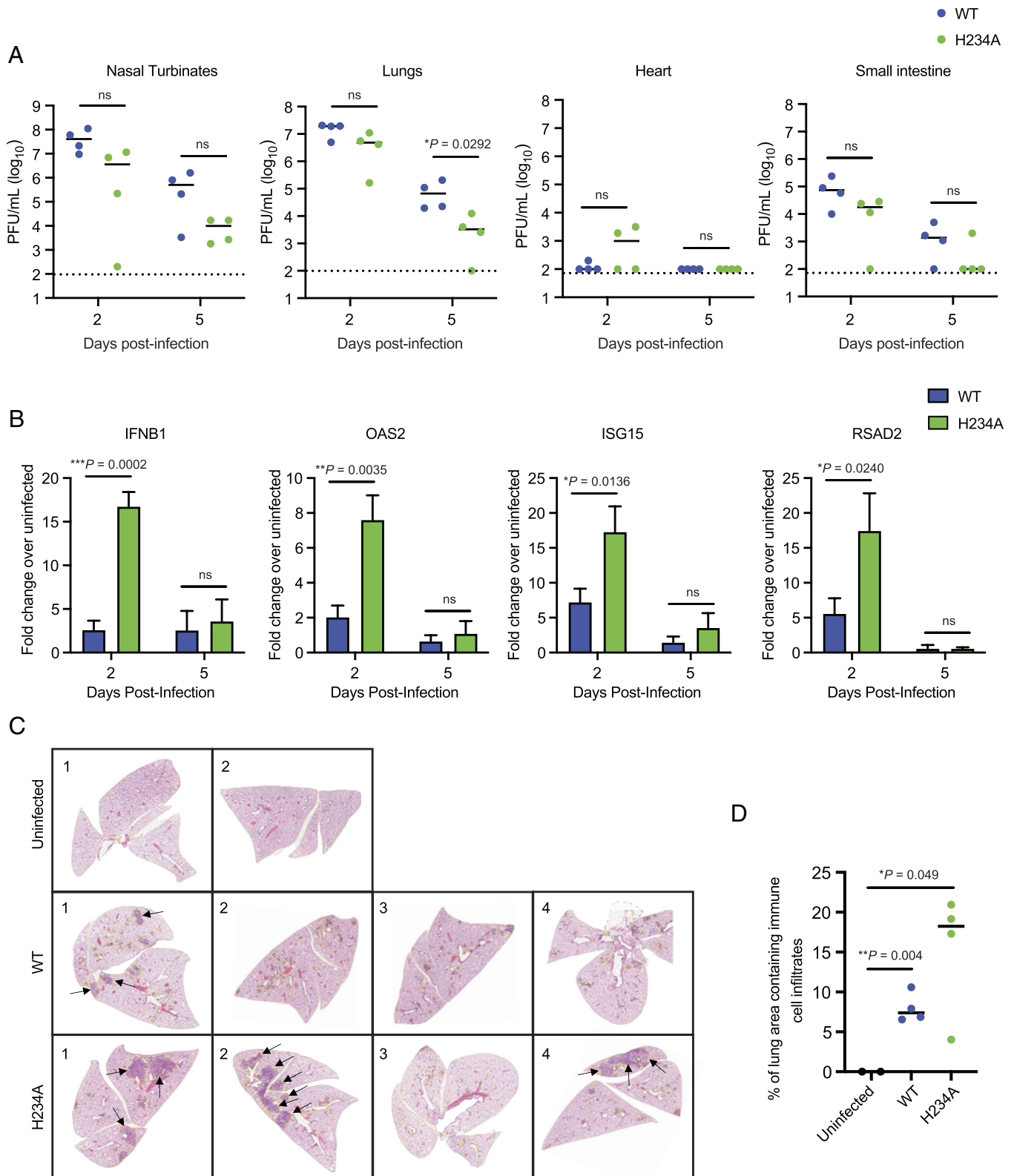


Fig. 4. The endoU catalytic mutant H234A replicates less efficiently and elicits higher immune responses in the lungs of hamsters. Syrian hamsters were intranasally inoculated with 1×10^3 PFU of WT virus ($n = 8$), H234A virus ($n = 8$), or with 100 μ L of 1X PBS ($n = 4$). Half of the animals were killed on day 2 and the rest on day 5 postinfection, and their nasal turbinates, lungs, heart, and small intestine were harvested. (A) Viral titers were measured by the plaque assay on Caco-2/AT cells. (B) Expression of indicated genes in the lungs was measured by RT-qPCR. (C) Images of H&E-stained lung tissues collected at 5 dpi. Black arrows indicate foci of immune cell infiltrates. (D) The percent area of lung scans containing immune cell infiltrates was measured as detailed in the *Materials and Methods* section. Statistical significance was determined using the two-tailed parametric *t* test.

SARS-CoV-2 encodes several proteins that antagonize the innate immune system, yet the loss of endoU activity significantly compromised the virus's immune-evasion capacity, indicating that

endoU is one of the most potent SARS-CoV-2 innate immune antagonists. Although endoU is thought to restrict innate immune activation by regulating dsRNA levels, direct experimental

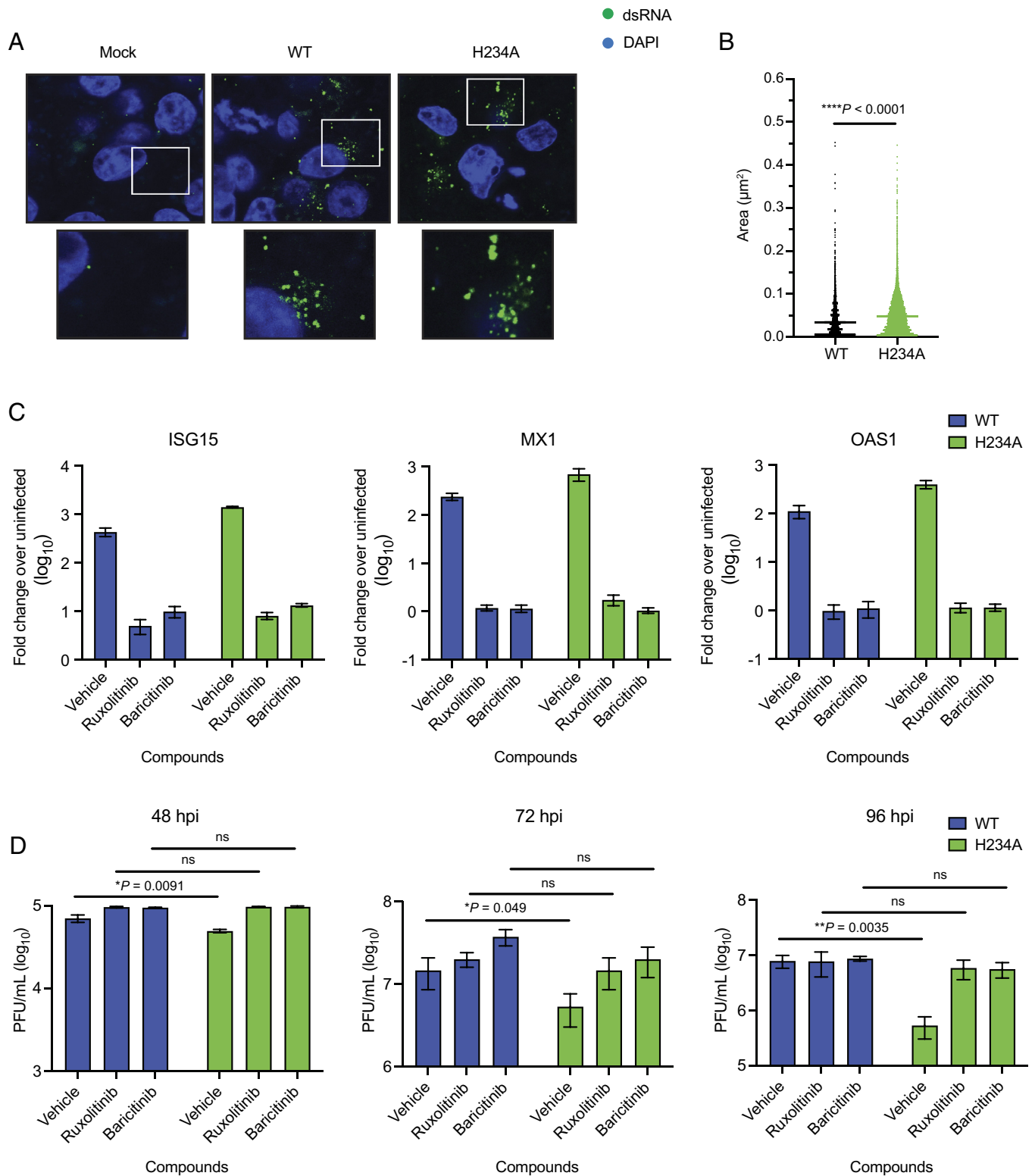


Fig. 5. The endoU catalytic mutant H234A elicits increased accumulation of dsRNA in infected cells. (A) iAT2 cells infected with indicated viruses at an MOI of 0.3 were stained with anti-dsRNA antibody (green). Nuclei were counterstained with DAPI (blue). Representative images are shown. (B) Quantification of area per punctum. 5,640 puncta for WT virus and 12,809 puncta for H234A virus were quantified in two fields across 27–41 Z planes of iAT2 cells infected at an MOI of 0.3 for 48 h. (C) Gene expression in iAT2 cells infected at an MOI of 0.3 for 48 h in the presence or absence of 10 μM compounds was analyzed by RT-qPCR. (D) Virus titer in apical washes collected from iAT2 cells grown in the presence or absence of 10 μM compounds for indicated times was measured by the plaque assay on Caco-2/AT cells. Statistical significance was determined using the two-tailed parametric *t* test.

evidence is lacking. The physiological substrates of endoU in infected cells, along with its temporal and spatial regulation, remain unknown. Key questions include whether nsp15 primarily targets ssRNA or dsRNA in cells, whether this targeting occurs within replication organelles, and how the extent and specificity

of RNA cleavage is regulated. Biochemical studies show that nsp15 can cleave both ss- and dsRNA (25, 47), but which of these species is predominantly targeted during infection is unclear. It is likely that nsp15 targets both dsRNAs and long viral ssRNA with short dsRNA motifs. A recent computational model suggests nsp15 acts

as a scaffold for the RTC, positioning it near viral RNA. It is plausible that nsp15 cleaves viral RNA within replication organelles, preventing RNA spillover into the cytoplasm where it could activate PRRs and trigger immune responses. Additionally, it is unclear whether endoU targets host RNAs and what determines its substrate specificity. Addressing these questions is critical for understanding how SARS-CoV-2 and other coronaviruses evade or suppress innate immune responses to optimize their replication and will inform the development of antivirals and live-attenuated vaccines for SARS-CoV-2 and related respiratory coronaviruses.

Materials and Methods

Biocontainment. All experiments were conducted in a state-of-the-art biosafety level 3 (BSL-3) laboratory at Boston University's National Emerging Infectious Diseases Laboratories (NEIDL) and Washington University in St Louis, adhering to biosafety protocols sanctioned by Institutional Biosafety Committees (IBC) of these institutions. The research was performed by scientists who had undergone extensive training in biosafety, biosecurity, and BSL-3 protocols before engaging in any experiments. Also, all Boston University researchers were medically cleared by the Boston University Research Occupational Health Program.

SARS-CoV-2 nsp15 Protein Purification. The codon-optimized SARS-CoV-2 nsp15 sequence (GenScript) was cloned into a pET46 bacterial expression vector containing an N-terminal 10X His-tag and a TEV cleavage site. The nsp15 mutants H234A, K289A, and S293A were generated by site-directed mutagenesis using the WT SARS-CoV-2 nsp15 construct as the template. C41 *Escherichia coli* cells were used for protein purification. Additional details are provided in *SI Appendix*.

In Vitro RNA Cleavage Assay. Purified proteins were incubated with a 16nt ssRNA substrate containing a 5' fluorescent tag and a single uridine cleavage site (FAM-GAAGCGAACCCUAAG) for 2 h at 33 °C. The reaction contained 1X cleavage assay buffer (10 mM Tris, 10 mM NaCl, pH 7.5), 1 mM DTT, 5 mM MnCl₂, and proteins mixed with 250 nM of RNA at 1:1, 1:2, 1:5, or 1:10 ratios. The reactions were stopped using an RNA loading buffer containing formamide, EDTA, and xylene cyanol. The samples were run on 8 M urea 15% PAGE for 1 h at 220 V and imaged with a Typhoon 9000 PLA imager to image the 5' cleavage products.

Cells, Antibodies, and Reagents. Details of the cells, antibodies, and reagents used in this study are provided in *SI Appendix*.

Generation of Recombinant SARS-CoV-2 by CPER. We employed the circular polymerase extension reaction (CPER) to generate recombinant SARS-CoV-2, using our previously published protocol (48). Further details are provided in *SI Appendix*.

Infection of iAT2 Cells. iAT2 cells were generated from our previously published SPC2-ST-B2 iPSC line (49, 50) and infected using our previously published protocol (29). Briefly, the cells grown as ALI cultures were infected with SARS-CoV-2 viruses, concentrated and partially purified by passing through a 20% sucrose cushion, to obtain an MOI of 0.3 (based on the titration performed on Caco-2 cells overexpressing hACE2 and human transmembrane protease, serine 2 (hTMPRSS2) Caco-2/AT cells). A 50 µL virus inoculum prepared in 1 × Dulbecco's phosphate-buffered saline (DPBS) (or 1x DPBS only for mock infection) was added to the apical side of cells and incubated for 2 h at 37 °C, followed by the removal of the inoculum and washing of the apical side of cells three times with 1 × DPBS (100 µL per wash). The apical washes were collected on different days of infection by adding 100 µL of 1 × DPBS to the apical side of cells and incubating at 37 °C for 15 min. The number of infectious virus particles in apical washes was measured by the plaque assay on Caco-2/AT cells. For protein extraction for western blot, iAT2 cells were lysed in the RIPA Lysis and Extraction Buffer (Thermo Scientific; #89900). Trizol (Invitrogen; #15596026) was used to extract RNA for RT-qPCR.

Animal Handling, Maintenance, and Infection.

K18-hACE2 Mice. All experimental protocols were approved by the Boston University Institutional Animal Care and Use Committee (PROTO202000020). The mice were housed in a facility accredited by the Association for the Assessment and Accreditation of Laboratory Animal Care (AAALAC). The heterozygous

K18-hACE2 C57BL/6 J mice (strain: 2B6.Cg-Tg(K18-ACE2)2Prln/J) of both sexes were acquired from Jackson Laboratory (Jax, Bar Harbor, ME). The animals were group-housed by sex in Tecniplast Green Line individually ventilated cages (Tecniplast, Buguggiate, Italy) under controlled conditions, with 30 to 70% humidity and a 12-h light/dark cycle. They had ad libitum access to both standard chow diets (LabDiet, St. Louis, MO) and water. The infection details are provided in *SI Appendix*.

Syrian hamsters. Hamster studies were conducted in accordance with the recommendations in the *Guide for the Care and Use of Laboratory Animals* of the NIH. The protocol was approved by the Institutional Animal Care and Use Committee at the Washington University School of Medicine (assurance number A3381-01). Forty male hamsters (5 to 6 wk old) were obtained from Charles River Laboratories and housed at Washington University in an enhanced Biosafety level 3 laboratory. Additional details are provided in *SI Appendix*.

Quantitative Real-Time PCR (RT-qPCR). RNA isolated from cells or tissues was used for cDNA synthesis with the ReadyScript cDNA Synthesis Mix (Sigma-Aldrich; #RDRT-25RXN). This cDNA served as the template for RT-qPCR. Briefly, a 20 µL of reaction mixture was prepared, containing 10 ng of cDNA, 0.75 µM of each forward and reverse primer, and 10 µL of the 2X Luna Universal One-Step Reaction Mix (New England Biolabs; #M3003S). Data were acquired using a QuantStudio3 Real-Time PCR System (Applied Biosystems) under the following conditions: an initial denaturation at 95 °C for 10 min, followed by 40 cycles of denaturation at 95 °C for 15 s, and annealing/extension at 60 °C for 1 min. A melt curve analysis of the PCR product was conducted from 65 °C to 95 °C, increasing by 0.5 °C per second, with a 30-s hold at 65 °C and a 5-s hold at each subsequent step, acquiring fluorescence at each temperature increment. Ct values were determined using QuantStudio™ Design and Analysis software V1.5.1. RPS11 was used as the housekeeping gene. The primers used are listed in *SI Appendix, Table S1*. The 2^{-ΔΔCt} method was applied as a relative quantification strategy for qPCR data analysis in Microsoft Excel. The calculated fold-change results, relative to either mock or WT, were graphed and analyzed using GraphPad Prism 10.

Flow cytometry. For detection of SARS-CoV-2 N by flow cytometry, uninfected and infected cells, fixed in 4% paraformaldehyde, were permeabilized in the Cytofix/Cytoperm buffer from the BD Cytofix/Cytoperm Fixation/Permeabilization kit (BD Biosciences; # 554714) for 15 min at RT. The cells were then washed once in 1 × Cytoperm/Cytowash buffer and stained with SARS-CoV-2 nucleocapsid antibody (Rockland; #200-401-A50, 1:2,000) for 1 h at RT. Following three washes in 1 × Cytoperm/Cytowash buffer, the cells were incubated with donkey anti-rabbit IgG-AF647 secondary antibody (ThermoFisher Scientific; #A-31573). Gating was based on uninfected control cells. Data were collected using a BD LSR II flow cytometer (BD Biosciences, CA) and analyzed with FlowJo v10.6.2 (FlowJo, Tree Star Inc).

Confocal microscopy. Cell staining for confocal microscopy was performed as described in our previous publication (30). Briefly, virus-infected iAT2 cells grown on transwells were fixed in 4% paraformaldehyde, permeabilized with 0.1% Triton X-100 in PBS, and blocked with a buffer containing 0.1% Triton X-100, 10% goat serum, and 1% BSA. Cells were incubated overnight at 4 °C with anti-dsRNA antibodies, followed by staining with secondary antibodies at room temperature for 1 h in the dark and counterstained with DAPI. Images were acquired at 60X on a Nikon Ti2 Eclipse microscope across at least 130 Z-planes, each 150 nm thick. Two microscopic fields were captured per well. Stacks were generated by including every 5th Z plane (750 nm thick) to minimize double counting puncta. Signals were normalized to uninfected cells to exclude background noise. Stacks were analyzed in ImageJ using the difference of Gaussians (DoG) feature enhancement algorithm.

Transcriptomic analysis of cells. Total RNA was extracted from iAT2 cells infected with SARS-CoV-2 at 24 and 48 hpi, along with time-matched uninfected controls, using Trizol reagent. All conditions were performed in biological triplicates. The samples were then sent to BGI Genomics (Cambridge, MA) for library preparation and sequencing (Paired-end, 150 bp, 20 M reads per sample). Raw read quality was examined using *FastQC* (51), and the quality trimming was performed using *BBduk* (52). Clean reads were mapped to the Genome Reference Consortium Human Build 38 (GRCh38, accessed from the Ensembl database <http://www.ensembl.org/>) using *STAR* (53) and to the SARS-CoV-2 genome using *BWA-MEM* (54). Raw gene counts were generated with *FeatureCounts* (55). Differentially expressed genes (DEGs) were identified using the R package *DESeq2* (56). First, genes with fewer than 10 raw counts or present

in less than three samples were discarded. The filtered raw gene count matrix was used to obtain DEGs, identified by comparing the gene-normalized count in WT and nsp15 mutant-infected samples to mock samples. DEGs were defined as those with a fold change gene expression greater than 4 and an adjusted *p*-value of less than 0.01. The DEG profiles were then used to predict associated Gene Ontology Terms using the Gene Set Enrichment Analysis analysis in the R package *clusterProfiler* (57). DEGs enriched in GO:0051607 (Defense Response to Virus) in each strain were visualized by their fold changes compared to mock using the R package *heatmap* (58).

Proteomic analysis of cells. SARS-CoV-2-infected iAT2 cells, along with time-matched uninfected controls, were harvested in biological triplicates at 48 and 72 hpi. The cells were detached by incubating with Accutase at 37 °C for 30 min. Subsequently, the cells were transferred to 1.5 mL Eppendorf tubes and centrifuged at 300×*g* for 5 min. The cell pellet was washed with 1× DPBS and lysed in a lysis buffer consisting of 1% sodium deoxycholate (SDC) in 100 mM Tris pH 8 and × protease inhibitor (Sigma-Aldrich; #11836170001). The proteins were reduced and alkylated with 10 mM TCEP and 40 mM CAA, respectively, boiled for 5 min at 95 °C, and sonicated in a Bioruptor (Diagenode) for 10 cycles of 30 s on/30 s off. The samples were digested overnight with a 1:100 (w/w) Trypsin/Lys-C Mix (Promega; #V5071) at 37 °C. Samples were acidified with TFA, centrifuged at 18,000×*g* for 10 min, approximately 150 ng of peptides were loaded onto pre-conditioned EvoTips (EvoSep), and washed following manufacturer instructions. Details of LC-MS/MS and data analysis are provided in *SI Appendix*.

Data, Materials, and Software Availability. The transcriptomics data have been uploaded to NCBI under the BioProject Accession [PRJNA1162484](https://doi.org/10.1101/2023.11.128), which can be viewed in read-only format using the following link: <https://dataview.ncbi.nlm.nih.gov/object/PRJNA1162484?reviewer=815gsk0fg9au15kgcal2i18ke0>.

1. G. Wolff *et al.*, A molecular pore spans the double membrane of the coronavirus replication organelle. *Science* **369**, 1395–1398 (2020).
2. S. Ricciardi *et al.*, The role of NSP6 in the biogenesis of the SARS-CoV-2 replication organelle. *Nature* **606**, 761–768 (2022).
3. X. Deng, S. C. Baker, An "Old" protein with a new story: Coronavirus endoribonuclease is important for evading host antiviral defenses. *Virology* **517**, 157–163 (2018).
4. A. Zheng *et al.*, Insight into the evolution of nidovirus endoribonuclease based on the finding that nsp15 from porcine deltacoronavirus functions as a dimer. *J. Biol. Chem.* **293**, 12054–12067 (2018).
5. J. Athmer *et al.*, In situ tagged nsp15 reveals interactions with coronavirus replication/transcription complex-associated proteins. *MBio* **8**, e02320–02316 (2017).
6. W. Xu *et al.*, Compartmentalization-aided interaction screening reveals extensive high-order complexes within the SARS-CoV-2 proteome. *Cell Rep.* **36**, 109482 (2021).
7. J. K. Perry *et al.*, An atomistic model of the coronavirus replication-transcription complex as a hexamer assembled around nsp15. *J. Biol. Chem.* **297**, 101218 (2021).
8. X. Deng *et al.*, Coronavirus nonstructural protein 15 mediates evasion of dsRNA sensors and limits apoptosis in macrophages. *Proc. Natl. Acad. Sci. U. S. A.* **114**, E4251–E4260 (2017).
9. X. Deng *et al.*, Coronavirus endoribonuclease activity in porcine epidemic diarrhea virus suppresses type I and type III interferon responses. *J. Virol.* **93**, e02000–02018 (2019).
10. M. Hackbart, X. Deng, S. C. Baker, Coronavirus endoribonuclease targets viral polyuridine sequences to evade activating host sensors. *Proc. Natl. Acad. Sci. U. S. A.* **117**, 8094–8103 (2020).
11. E. Kindler *et al.*, Early endonuclease-mediated evasion of RNA sensing ensures efficient coronavirus replication. *PLoS Pathog.* **13**, e1006195 (2017).
12. J. Zhao *et al.*, Coronavirus endoribonuclease ensures efficient viral replication and prevents protein kinase R activation. *J. Virol.* **95**, e02103–02120 (2021).
13. C. J. Otter *et al.*, SARS-CoV-2 nsp15 endoribonuclease antagonizes dsRNA-induced antiviral signaling. *Proc. Natl. Acad. Sci. U. S. A.* **121**, e2320194121 (2024).
14. M. C. Pillon *et al.*, Cryo-EM structures of the SARS-CoV-2 endoribonuclease Nsp15 reveal insight into nuclease specificity and dynamics. *Nat. Commun.* **12**, 636 (2021).
15. K. Bhardwaj, L. Guarino, C. C. Kao, The severe acute respiratory syndrome coronavirus Nsp15 protein is an endoribonuclease that prefers manganese as a cofactor. *J. Virol.* **78**, 12218–12224 (2004).
16. K. Bhardwaj *et al.*, Structural and functional analyses of the severe acute respiratory syndrome coronavirus endoribonuclease Nsp15. *J. Biol. Chem.* **283**, 3655–3664 (2008).
17. M. N. Frazier *et al.*, Characterization of SARS2 Nsp15 nuclease activity reveals it's mad about U. *Nucleic Acids Res.* **49**, 10136–10149 (2021).
18. Y. Kim *et al.*, Crystal structure of Nsp15 endoribonuclease NendoU from SARS-CoV-2. *Protein Sci.* **29**, 1596–1605 (2020).
19. L. A. Guarino *et al.*, Mutational analysis of the SARS virus Nsp15 endoribonuclease: Identification of residues affecting hexamer formation. *J. Mol. Biol.* **353**, 1106–1117 (2005).
20. Y. Kim *et al.*, Tipiracil binds to uridine site and inhibits Nsp15 endoribonuclease NendoU from SARS-CoV-2. *Commun. Biol.* **4**, 193 (2021).
21. Z. M. Wright *et al.*, Spontaneous base flipping helps drive Nsp15's preferences in double stranded RNA substrates. *Nat. Commun.* **16**, 391 (2025).
22. M. Saramago *et al.*, The nsp15 nuclease as a good target to combat SARS-CoV-2: Mechanism of action and its inactivation with FDA-approved drugs. *Microorganisms* **10**, 342 (2022).
23. T. Huang *et al.*, Kinetic analysis of RNA cleavage by coronavirus Nsp15 endonuclease: Evidence for acid-base catalysis and substrate-dependent metal ion activation. *J. Biol. Chem.* **299**, 104787 (2023).

[nih.gov/object/PRJNA1162484?reviewer=815gsk0fg9au15kgcal2i18ke0](https://doi.org/10.1101/2023.11.128). The mass spectrometry proteomics data files are deposited to the ProteomeXchange Consortium (59), via the PRIDE partner repository with the Accession ID [PXD056702](https://doi.org/10.26434/chemrxiv-2023-pxd05).

ACKNOWLEDGMENTS. This work was supported by NIH R01 AI159945 (to R.N.K., M.S., and S.C.B.), NIH P01 HL170952 (K.D.A. and D.N.K.), NIH N01 75N92020C00005 (D.N.K.), and NIH S100D030269 (N.A.C.). A.C. received support from NIH T32 HL007035, C.M.B. from Swedish Research Council (2023-00510), M.E. from NIH T32 AI007508, K.D.A. from NIH K08 HL163494 and a Boston University School of Medicine Department of Medicine Career Investment Award, and M.S. from Boston University Startup funds.

Author affiliations: ^aDepartment of Biochemistry and Cell Biology, Boston University Chobanian and Avedisian School of Medicine, Boston, MA 02118; ^bNational Emerging Infectious Diseases Laboratories, Boston University, Boston, MA 02118; ^cDepartment of Pathology and Laboratory Medicine, Emory University School of Medicine, Atlanta, GA 30322; ^dDepartment of Surgical Sciences, Uppsala University, Uppsala 75185, Sweden; ^eDepartment of Medicine, Washington University School of Medicine, St. Louis, MO 63110; ^fDepartment of Pathology and Immunology, Washington University School of Medicine, St. Louis, MO 63110; ^gDepartment of Molecular Microbiology, Washington University School of Medicine, St. Louis, MO 63110; ^hDepartment of Microbiology and Immunology, Loyola University Chicago Stritch School of Medicine, Maywood, IL 60153; ⁱThe Pulmonary Center, Boston University Chobanian and Avedisian School of Medicine, Boston, MA 02118; ^jDepartment of Virology, Immunology, and Microbiology, Boston University Chobanian and Avedisian School of Medicine, Boston, MA 02118; ^kDepartment of Biochemistry, Institute for Molecular Virology, Center for Quantitative Cell Imaging, University of Wisconsin-Madison, Madison, WI 53706; ^lCenter for Regenerative Medicine, Boston University and Boston Medical Center, Boston, MA 02118; ^mThe Department of Medicine, Boston University Chobanian and Avedisian School of Medicine, Boston, MA 02118; and ⁿDepartment of Pathology and Laboratory Medicine, Boston University Chobanian and Avedisian School of Medicine, Boston, MA 02118

24. I. Salukhe, R. Choi, W. Van Voorhis, L. Barrett, J. Hyde, Regulation of coronavirus nsp15 cleavage specificity by RNA structure. *PLoS ONE* **18**, e0290675 (2023).
25. M. N. Frazier *et al.*, Flipped over U: Structural basis for dsRNA cleavage by the SARS-CoV-2 endoribonuclease. *Nucleic Acids Res.* **50**, 8290–8301 (2022).
26. J. Desmyter, J. L. Melnick, W. E. Rawls, Defectiveness of interferon production and of rubella virus interference in a line of African green monkey kidney cells (Vero). *J. Virol.* **2**, 955–961 (1968).
27. J. D. Mosca, P. M. Pitha, Transcriptional and posttranscriptional regulation of exogenous human beta interferon gene in simian cells defective in interferon synthesis. *Mol. Cell. Biol.* **6**, 2279–2283 (1986).
28. M. Carcatera, C. Caruso, Alveolar epithelial cell type II as main target of SARS-CoV-2 virus and COVID-19 development via NF-Kb pathway deregulation: A physio-pathological theory. *Med. Hypotheses* **146**, 110412 (2021).
29. J. Huang *et al.*, SARS-CoV-2 infection of pluripotent stem cell-derived human lung alveolar type 2 cells elicits a rapid epithelial-intrinsic inflammatory response. *Cell Stem Cell* **27**, e967 (2020).
30. D. Y. Chen *et al.*, SARS-CoV-2 disrupts proximal elements in the JAK-STAT pathway. *J. Virol.* **95**, e0086221 (2021).
31. H. Jeong *et al.*, Comparison of the pathogenesis of SARS-CoV-2 infection in K18-hACE2 mouse and Syrian golden hamster models. *Dis. Model. Mech.* **15**, dmm049632 (2022).
32. R. D. Jiang *et al.*, Pathogenesis of SARS-CoV-2 in transgenic mice expressing human angiotensin-converting enzyme 2. *Cell* **182**, e58 (2020).
33. L. Bao *et al.*, The pathogenicity of SARS-CoV-2 in hACE2 transgenic mice. *Nature* **583**, 830–833 (2020).
34. F. S. Oladunni *et al.*, Lethality of SARS-CoV-2 infection in K18 human angiotensin-converting enzyme 2 transgenic mice. *Nat. Commun.* **11**, 6122 (2020).
35. M. Imai *et al.*, Syrian hamsters as a small animal model for SARS-CoV-2 infection and countermeasure development. *Proc. Natl. Acad. Sci. U. S. A.* **117**, 16587–16595 (2020).
36. K. Rosenke *et al.*, Defining the Syrian hamster as a highly susceptible preclinical model for SARS-CoV-2 infection. *Emerg. Microbes Infect.* **9**, 2673–2684 (2020).
37. Y. Arai *et al.*, Stimulation of interferon-beta responses by aberrant SARS-CoV-2 small viral RNAs acting as retinoic acid-inducible gene-I agonists. *iScience* **26**, 105742 (2023).
38. T. Zhou *et al.*, Generation and functional analysis of defective viral genomes during SARS-CoV-2 infection. *MBio* **14**, e0025023 (2023).
39. R. N. Kirchoefer, A. B. Ward, Structure of the SARS-CoV nsp12 polymerase bound to nsp7 and nsp8 co-factors. *Nat. Commun.* **10**, 2342 (2019).
40. C. E. Comar *et al.*, MERS-CoV endoribonuclease and accessory proteins jointly evade host innate immunity during infection of lung and nasal epithelial cells. *Proc. Natl. Acad. Sci. U. S. A.* **119**, e2123208119 (2022).
41. R. Ancar *et al.*, Physiological RNA targets and refined sequence specificity of coronavirus endo-RNA **26**, 1976–1999 (2020).
42. B. Gao *et al.*, Inhibition of anti-viral stress granule formation by coronavirus endoribonuclease nsp15 ensures efficient virus replication. *PLoS Pathog.* **17**, e1008690 (2021).
43. S. Li *et al.*, SARS-CoV-2 Z-RNA activates the ZBP1-RIPK3 pathway to promote virus-induced inflammatory responses. *Cell Res.* **33**, 201–214 (2023).
44. R. Karki *et al.*, ZBP1-dependent inflammatory cell death, PANoptosis, and cytokine storm disrupt IFN therapeutic efficacy during coronavirus infection. *Sci. Immunol.* **7**, eab06294 (2022).
45. C. Yin, S. Balachandran, ZBP1 inflames the SARS-CoV-2-infected lung. *Cell Res.* **33**, 333–334 (2023).
46. M. Evdokimova *et al.*, Coronavirus endoribonuclease antagonizes ZBP1-mediated necroptosis and delays multiple cell death pathways. *Proc. Natl. Acad. Sci. U. S. A.* **122**, e2419620122 (2025).

47. X. Wang, B. Zhu, SARS-CoV-2 nsp15 preferentially degrades AU-rich dsRNA via its dsRNA nickase activity. *Nucleic Acids Res.* **52**, 5257–5272 (2024).
48. D. Y. Chen *et al.*, Cell culture systems for isolation of SARS-CoV-2 clinical isolates and generation of recombinant virus. *iScience* **26**, 106634 (2023).
49. K. D. Alysandratos *et al.*, Patient-specific iPSCs carrying an SFPC mutation reveal the intrinsic alveolar epithelial dysfunction at the inception of interstitial lung disease. *Cell Rep.* **36**, 109636 (2021).
50. K. Hurley *et al.*, Reconstructed single-cell fate trajectories define lineage plasticity windows during differentiation of human PSC-derived distal lung progenitors. *Cell Stem Cell* **26**, e598 (2020).
51. S. Andrew, FastQC: A quality control tool for high throughput sequence data. *Analyt. Biochem.* **548**, 38–43 (2010).
52. B. Bushnell, BBTools software package (2014). <https://sourceforge.net/projects/bbmap/>. Accessed 5 February 2024.
53. A. Dobin *et al.*, STAR: Ultrafast universal RNA-seq aligner. *Bioinformatics* **29**, 15–21 (2013).
54. H. Li, Aligning sequence reads, clone sequences and assembly contigs with BWA-MEM. *arXiv[Preprint]* (2013). <https://doi.org/10.48550/arXiv.1303.3997> (Accessed 5 February 2024).
55. Y. Liao, G. K. Smyth, W. Shi, featureCounts: An efficient general purpose program for assigning sequence reads to genomic features. *Bioinformatics* **30**, 923–930 (2014).
56. M. I. Love, W. Huber, S. Anders, Moderated estimation of fold change and dispersion for RNA-seq data with DESeq2. *Genome Biol.* **15**, 550 (2014).
57. T. Wu *et al.*, ClusterProfiler 4.0: A universal enrichment tool for interpreting omics data. *Innovation (Camb.)*, **2**, 100141 (2021).
58. R. Kolde, pheatmap: Pretty Heatmaps (2018). <https://cran.r-project.org/web/packages/pheatmap/pheatmap.pdf>. Accessed 5 February 2024.
59. J. A. Vizcaino *et al.*, ProteomeXchange provides globally coordinated proteomics data submission and dissemination. *Nat. Biotechnol.* **32**, 223–226 (2014).